

ABSTRACT

I present the results of a time series analysis of ground-based optical photometric monitoring of Mrk 841. The light curves have a nearly daily cadence with some gaps from 2016 March to 2017 August in 5 filters (V and $g'r'i'z_s$). With these disc reverberations, combined with contemporaneous ultraviolet data from *Swift*, I confirm significant time delays between the continuum bands as a function of wavelength from the UVW2 band to the z band. I find that the measured lags at each band vary greatly with frequency, explicable by disc transfer function asymmetry and broad-line region (BLR) effects. I also find that lags at the z band are comparable to those at the i band, suggestive of BLR influence. The trend of lag τ with wavelength λ , if purely fitted to the power law relation $\tau \propto \lambda^{4/3}$, imply a disc radius that is 3 times larger than the prediction for a standard geometrically thin, optically thick, centrally illuminated disc. I find that inclusion of the diffuse continuum emission from the BLR reduces this mismatch. Decomposing the flux into constant and variable components, a flux-flux analysis shows a variable spectrum that follows $f_\nu \propto \lambda^{-1/3}$, as expected for a disc. Using the faint variable fluxes in each UV/optical band, I combine them with *Swift* X-ray spectra to fit spectral energy distribution (SED) models. I also report the insights into the geometry and characteristics of Mrk 841 as it relates to these models.

1 INTRODUCTION

Supermassive black holes (SMBH) are at the centre of nearly every galaxy in the known universe (Schneider 2015). When SMBH are accreting mass (usually gas, and by means of an accretion disc), they are called active galactic nuclei (AGN hereafter; King & Pringle 2007). AGN are understood to play an important role in their host galaxies as they can influence their development by means of AGN feedback such as winds and outflows (Silk & Rees 1998; Fabian 1999). Therefore, understanding the accretion process as well as the geometry and structure of AGN will provide greater insight into galaxy evolution as well as black holes in general.

Currently, the continuum emission of AGNs are believed to originate from the accretion disc surrounding the SMBHs. These accretion discs are generally believed to be geometrically thin and optically thick (Shakura & Sunyaev 1973) and when modelled using accretion rates and masses appropriate for SMBHs, yield maximum temperatures of $\sim 10^5 - 10^6$ K.

In Fig. 1, modified from Cackett et al. (2021), it is shown how obtained fluxes inform the geometric modelling of accretion discs. Essentially, when fitting a physical model to the spectral energy distribution (SED) of AGN, it is possible to recover the geometry of the disc within the parameters of the model. Thus, it is essential to produce as accurate as a model as possible in order to truly understand AGN.

1.1 Reverberation mapping

In most cases, AGN are too small to spatially resolve even with modern telescopes (Peterson & Horne 2004; Cackett et al. 2021). Instead, reverberation mapping, first described by Blandford & McKee (1982), is used as it relies upon time resolution rather than spatial resolution. As material accretes onto the AGN, energy is released, which causes changes in the observed brightness that propagate outwards at the speed of light. As light travels outwards and farther

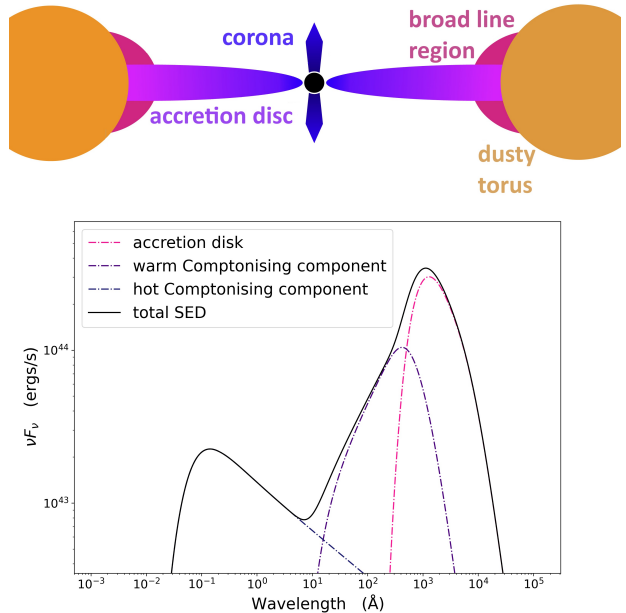


Figure 1. Top: Cross-sectional schematic of an AGN, adapted from Cackett et al. (2021). It also illustrates the length-scales of the different structures as well as labelling each structure with the method used to observe it. Bottom: Example of a relativistic AGN SED model RELAGN (Hagen & Done 2023) with its components' origins labelled. X-ray photons are emitted from the corona, the cause of the hot Comptonizing component of the SED. They are then reprocessed at different regions in the disc with the distance to each region introducing time lags. In this SED model, the inner disc produces the warm Comptonizing component with a puffed up disc and the outer disc is modelled as a simpler standard geometrically thin, optically thick disc.

from the AGN, it may be absorbed and then reprocessed at different wavelengths depending on the region of the disc, resulting in ‘echoes’. On Earth, these echoes are observed at different parts of the electromagnetic spectrum with an associated time lag that depends on which region of the accretion disc the signal originates from. This method relies upon a few key assumptions (for a more in-depth review see Peterson & Horne 2004; Cackett et al. 2021):

(i) There is only one central source of light: the corona of AGN, which is the cause of all observed variations in the light curve as it is the initial ionising flux all following variations reverberate.

(ii) The light travel time is the most important factor affecting the observed time lag. For this to be true, the recombination timescale must be irrelevant and the dynamical timescale relatively short. Thus, the time lag and the size of the accretion disc are only related by the speed of light: $\tau = R/c$.

(iii) There is a simple but not necessarily linear relationship between the ionising continuum and the reprocessed continuum. It is assumed that the reprocessed fluxes are simply a blurred and delayed copy of the initial ionising flux, allowing for simple cross-correlation between light curves at different wavelengths to obtain the time lag. The light curve response is also dependent on the temperature profile of the disc $T(R)$ and thus related to both the mass accretion rate \dot{M} and the radius of the disc R .

Under these assumptions, it is then possible to fit a model to the calculated time lag spectrum, and from the model parameters, obtain the desired parameters: the central black hole mass M_{BH} , the mass accretion rate \dot{M} , and the radius of the disc R to name a few.

For standard geometrically thin, optically thick, irradiated disc with no relativistic treatments, the standard temperature profile follows Eq. 1:

$$T(R) = \left(\frac{3GM_{\text{BH}}\dot{M}}{8\pi\sigma R^3} + \frac{(1-A)L_X H}{4\pi\sigma R^3} \right)^{1/4}, \quad (1)$$

where M_{BH} is the mass of the central SMBH, \dot{M} is the mass accretion rate of the disc, R is the distance away from the corona, L_X is the luminosity of the heating radiation, and A is the albedo of the disc (Cackett et al. 2007). In this equation, the inclination and the inner edge of the disc are ignored, which makes for large discrepancies at wavelengths $< 2000 \text{ \AA}$ (Novikov & Thorne 1973). While this does not cause much of an issue for UV/optical lags, it introduces significant errors for fitting lower-wavelength, higher-frequency, lags that originate from very close to the SMBH. As it is advantageous to get data in as high frequency of a wave band as possible, because this will naturally trace out more and more representative reverberations of the initial ionising flux, this is a problem. However, since it is not much of an issue within the UV/optical regime, it is perfectly suitable for use in Section 4 when modeling the lag spectrum.

As black body radiation is assumed ($\lambda \propto T^{-1}$ and thus $T = Xhc/k\lambda$), this leads to Eq. 2:

$$c\tau = R = \left(X \frac{k\lambda_0}{hc} \right)^{4/3} \left(\frac{3GM_{\text{BH}}\dot{M}}{8\pi\sigma} + \frac{(1-A)L_X H}{4\pi\sigma} \right)^{1/3}. \quad (2)$$

Measuring τ relative to a reference delay τ_0 given by the light curve of reference wavelength λ_0 , this leads to Eq. 3:

$$(\tau - \tau_0) = \frac{1}{c} \left(X \frac{k\lambda_0}{hc} \right)^{4/3} \left(\frac{3GM_{\text{BH}}\dot{M}}{8\pi\sigma} + \frac{(1-A)L_X H}{4\pi\sigma} \right)^{1/3} \times \left[\left(\frac{\lambda}{\lambda_0} \right)^{4/3} - 1 \right]. \quad (3)$$

The mass accretion rate \dot{M} can only be determined indirectly from the bolometric luminosity L_{Bol} . To further simplify Eq. 3, $L_{\text{Bol}} = \eta \dot{M} c^2 = \dot{m}_{\text{Edd}} L_{\text{Edd}}$ where η is the radiative efficiency for turning rest mass into radiative energy; \dot{m}_{Edd} is the Eddington ratio; and L_{Edd} is the Eddington luminosity. Additionally, $(1-A)L_X H/R = \kappa GM_{\text{BH}}\dot{M}/2R$ where κ is the local ratio to external to internal heating that is constant with radius. This leads to Eq. 4:

$$(\tau - \tau_0) = \frac{1}{c} \left(X \frac{k\lambda_0}{hc} \right)^{4/3} \left[\left(\frac{GM}{8\pi\sigma} \right) \left(\frac{L_{\text{Edd}}}{\eta c^2} \right) (3 + \kappa) \dot{m}_{\text{Edd}} \right]^{1/3} \times \left[\left(\frac{\lambda}{\lambda_0} \right)^{4/3} - 1 \right]. \quad (4)$$

as seen in Fausnaugh et al. (2016). Fitting this model to the lag spectrum of an AGN would theoretically allow for the recovery of the desired parameters, but that is not the case.

1.2 'Too-large' time lags

The standard accretion disc model is that of a geometrically thin optically thick disc vertically supported by thermal pressure as in Shakura & Sunyaev (1973). This disc reprocessing model predicts a $\tau \propto \lambda^{4/3}$ relation, as the variations from the smaller hotter inner disc are expected to occur before variations originating from the larger cooler outer disc. However, the measurements derived from observations frequently predict a time lag two to three times larger than what would be expected from the model (e.g. Edelson et al. 2019; Hernández Santisteban et al. 2020; Li et al. 2021; Guo et al. 2022). This means that the accretion disc's radius for a given temperature is generally larger than expected from this theory. Thus, some assumptions made previously could be wrong, such as ignoring inclination, relativistic effects, and the inner edge of the disc. However, Homayouni et al. (2019) shows that using only the best lag measurements biases the disc size measurements to be larger and when the full sample is used, there is generally less discrepancy. Additionally, previous studies have found cases where observations did match with the theory (e.g.

(Homayouni et al. 2019; Yu et al. 2020). This may mean that there are situations where this model is appropriate and might have been appropriate if not for improper analysis, although there have been many more cases where it hasn't been (e.g. Edelson et al. 2019; Hernández Santisteban et al. 2020; Li et al. 2021; Guo et al. 2022).

Over the years, there have been a variety of explanations for this discrepancy, ranging from different geometries of the accretion disc, alternative temperature profiles, and different models altogether. A theory that correctly reproduces the observed results has not yet been found. One model that this report will talk about is that of adding in the effects of the broad line region (BLR), an extended region of gas that sees an absorbed ionising continuum. In response, the BLR produces significant bound-free and free-free continuum emission, resulting in a spectrum that not only peaks at the Balmer and Paschen jumps (U band and $i'z_s$ bands respectively), but also across the UV/optical (Korista & Goad 2001; Netzer 2019). A contribution to the lags from the BLR diffuse continuum emission (DCE) could account for a large portion (or even all) of the disc size disparity.

1.3 Mrk 841

The focus of this report is the Seyfert 1 galaxy Mrk 841 (Markarian & Lipovetskii 1976). It is at redshift $z = 0.03642$ (Falco et al. 1999), with a central black hole $\log M/M_\odot = 8.00$ (Castelló-Mor et al. 2017). While it has been previously studied for its soft X-ray excess dimming (e.g. Nandra et al. 1995; Mehdipour et al. 2023) and its Fe K α line (Day et al. 1990; Longinotti et al. 2004; Petrucci et al. 2006, 2007), as well as had its BLR reverberation mapped (Brotherton et al. 2020), there has been no attempt yet made to use reverberation mapping to probe its accretion disc. In this report, the geometry of Mrk 841 has been characterised in detail for the first time, thus providing more evidence as to the nature and behaviour of AGN.

Using BLR reverberation mapping, Brotherton et al. (2020) characterises the SMBH mass of Mrk 841 as being $7.6 \pm 0.1 \log M_\odot$.

Additionally, Mehdipour et al. (2023) characterises Mrk 841 as similar to "changing-look AGN", an object that has its SED change by a dramatic amount within a span of time that should not allow for such extreme changes. Mehdipour et al. (2023) compared data collected in 2001 to data collected in 2022. As this project deals with data collected from 2016 March to 2017 August, it is well suited to explore the transitional period between the two states of Mrk 841 characterised by Mehdipour et al. (2023).

1.4 Report contents

This report is split into six major sections. In Section 2, I describe the observations and data reduction. Section 3 describes my time series analysis of the UV/optical light curves as well as the results of applying frequency resolved lag analysis. In Section 4 I fit lag spectrum models and discuss my results thereof. In Section 5, I show the decomposition of the UV/optical light curves into variable component fluxes and fit an SED model to the resultant spectra. I also compare my SED model to the models fitted by Mehdipour et al. (2023) and explain the results of that. In Section 6 I discuss the results of the SED model fitting. Finally, I summarise my key results in Section 7, with some suggestions for future work.

2 OBSERVATIONS

Mrk 841 was observed by the Las Cumbres Observatory global telescope network (LCO hereafter; Brown et al. 2013) in the period of 2016 March to 2017 August (MJD 57495–57962). Contemporaneously, Mrk 841 was also observed with the Neil Gehrels *Swift* Observatory (*Swift* hereafter; Gehrels et al. 2004) X-ray and UV/optical (UVOT) telescopes. From these observations, a multi-wavelength dataset ranging from the X-ray to the optical of Mrk 841 was obtained.

Swift monitored the target with an irregular cadence in the 0.3–10 keV X-rays and six broadband UV/optical filters (UVW2, UVM2, UVW1, U, B, V) spanning $\sim 1900 - 5500\text{\AA}$. However, only data in the UVW2 filter was used. LCO performed $g'Vr'i'z_s$ photometry approximately once per day. The results from these two instruments form the basis of this work.

2.1 Las Cumbres Observatory

A multi-wavelength light curve of Mrk 841 was obtained using the LCO network's 1-m robotic telescopes as part of the 2014A AGN Key project and accessed through the AGN Variability Archive (Hernández Santisteban 2024). It was observed in optical broadband filters Johnson/Cousins V and Sloan Digital Sky Survey (SDSS) $g'r'i'z_s$. Observations were obtained with a cadence of around 0.95 days, from the LCO sites at Teide (Spain), Cerro Tololo (Chile), MacDonald (Texas, USA), and Sliding Spring (Australia). Observations were taken using the Sinistro CCD camera. In total, 2454 individual exposures were taken in five bands: $g'Vr'i'z_s$.

The data accessed from the AVA archive were already data reduced according to the procedure outlined in Hernández Santisteban et al. (2020). A more detailed description is set out in Hernández Santisteban (2024). But broadly, the initial images were

pipeline processed to be bias and flat field with BAN-ZAI (McCully et al. 2022). Multi-aperture aperture photometry was performed on each image, and the background was subtracted. Then, stable light curves for the objects were produced by constructing a curve of growth for each image and fitting a point-spread-function to every star flux (Hernández Santisteban et al. 2020).

Data free of obvious errors were then further reduced, telescope intercalibrated, and photometrically calibrated using PyTICS (Vielute 2024). Mrk 841 was identified from the other field stars in the image through manual inspection of MJD-magnitude plots of the objects captured. It was able to be distinguished from the field stars because of the variations in the light curve, a signature characteristic of AGNs.

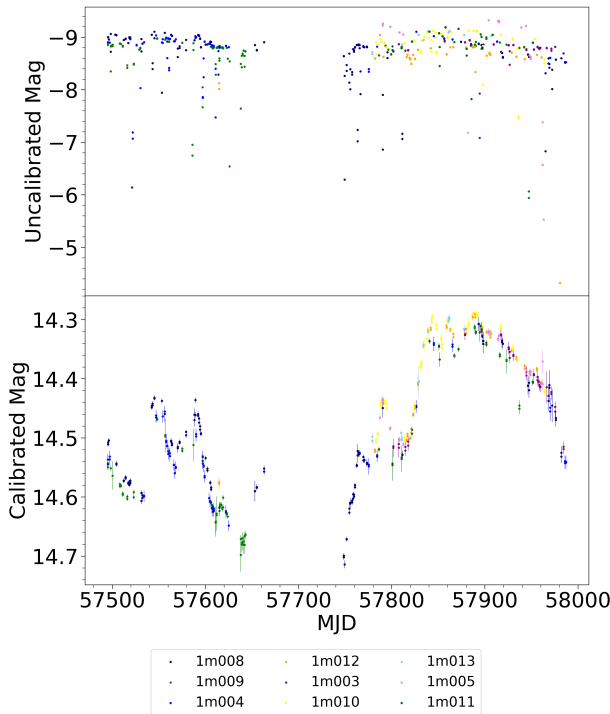


Figure 2. LCO g' -band light curve of Mrk 841 showing the data before and after the inter-telescope flux recalibration through PyTICS.

2.1.1 Intercalibration and reduction of LCO light curves

In order to combine light curves in the same filter but from different LCO telescopes, it is necessary to intercalibrate to a common flux scale to account for the variances between instruments. This is because although the telescope, detector, and filter sets use identical designs, there exist small systematic offsets which must be accounted for. This is seen in Fig. 2, which shows the g' band light curve of Mrk 841.

Without telescope intercalibration, there are significant systematic offsets between the different telescopes' light curves even though they all in the same band.

PyTICS (Vielute 2024) works by first separating the data by wave band, with unique identifiers noted for each telescope used. Then, using background comparison stars, the data is corrected for atmospheric variability. Systematic corrections are then made with extra variance parameters based on the field stars' scatter rather than making assumptions about the AGN light curve shape and adding variance parameters based on model deviations. This is done by fitting a model to all star data and then iteratively making corrections, intercalibrating between all telescopes simultaneously.

The fit is considered converged once the likelihood is maximised and a corrected calibrated light curve is the result. The reported uncertainties are quantified by adding in quadrature the star-specific intrinsic error, the epoch-specific error, and the telescope-specific calibration error.

The AAVSO Photometric All-Sky Survey (APASS; Henden et al. 2018) DR10 was used for all LCO filters to perform photometric calibration. Comparison stars in each field were used to perform a zero-point calibration at each epoch.

2.2 Swift - XRT

Data from two of Swift's three instruments are used in this paper: the X-Ray Telescope (XRT; Burrows et al. 2005) and the UV/optical telescope (UVOT; Roming et al. 2005). The XRT observations were made in photon counting (PC) mode and analysed using the standard Swift analysis tools as described in Evans et al. (2009). Those produced fully corrected spectra that have accounted for instrumental effects. The observation times specified were such that the spectral data would at least originate from the time period between 2016 March and 2017 August, if not at the exact same observation times as the photometric data from the LCO telescopes. In all other cases, the default values were used. This generated an X-ray light curve covering the full XRT bandpass (XF; 0.3–10 keV). For a more detailed discussion of this tool, please see Evans et al. (2009).

2.3 Swift - UVOT

Contemporaneous UVOT data for Mrk 841 was accessed through Gelbord J. (priv. comm.), whose data reduction method follows the same procedure as described in Hernández Santisteban et al. (2020). The process involves flux measurement, removal of failed points, and masking of low-sensitivity regions of

the detector, using the regions identified by Hernández Santisteban et al. (2020). As Mrk 841 does not have a blurred point-spread function (PSF), measurements were made using the standard 5"-radius extraction region described in Hernández Santisteban et al. (2020).

In the observation period specified (2016 March — 2017 August), only the UVW2 band was judged to have enough data points to construct a viable light curve. The reason for this is easily visible in Fig. 3.

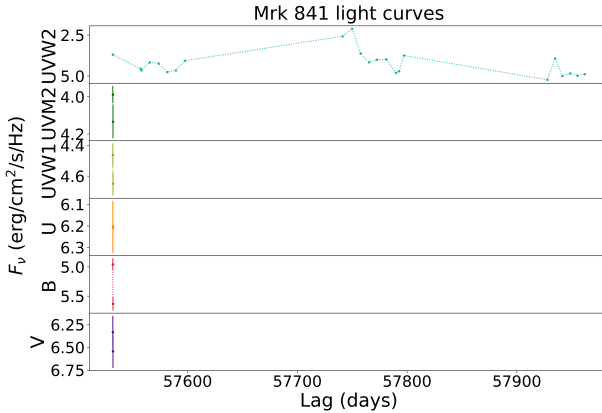


Figure 3. Contemporaneous (2016 March-2017 August) light curves of Mrk 841 from the *Swift* UV/optical telescope. Shown are the six UV/optical filters UVW2, UVM2, UVW1, U, B, V.

3 TIME SERIES ANALYSIS

The light curve time series obtained from the LCO network and *Swift* UVOT were analysed and cross-correlated to yield the time lags between each band and the reference. This is done because as discussed in Section 1.1, using this dataset, Mrk 841 is resolved in time and flux rather than spatially. With that resolution, it is then possible to recover how the light curves emitted from Mrk 841 vary as a function of time and thus distance from the central source.

The LCOT data ($g'Vr'i'z_s$) and the *Swift* UVOT data (UVW2) were manually combined into a single dataset to be measured jointly. As PyROA only works in fluxes, the absolute magnitudes of the LCOT data were converted into mJy.

3.1 PyCCF

A preliminary CCF measurement was made using PyCCF (Sun et al. 2018), the results of which are shown in Fig. 4. Due to the large gap in between the LCOT and UVOT data collected in 2016 and 2017, the dataset for each observation period had to be analysed separately as PyCCF is incapable of handling very large gaps in data. As the W2 band

was very sparse in data, the g' band is considered the reference band throughout and all other bands are considered subsidiary in this analysis.

The CCF was calculated between each of the light curves and the g' reference light curve from -50 to 50 days. For each CCF calculation, the peak and centroid of the CCF was also determined, with the centroid calculated only using points that are greater than 0.8 of the maximum CCF value. The median and 68% confidence intervals of the centroid and peak distributions were used to determine the lag peak, lag centroid, as well as their associated uncertainties.

The CCF measured with PyCCF is presented to the right-hand-side of the light curves in Fig. 4. In general, the lags increase with wavelength, roughly following $\tau \propto \lambda^{4/3}$. However, this trend does not hold for the UVW2 band during 2016 March-2016 September, most likely because there are so few data points available in that band that the CCF cannot be calculated properly when comparing the curve to the g' band since PyCCF only performs a linear interpolation between the gaps. This problem will be resolved in Section 3.2, as PyROA has been developed to use the properties of the light curves to perform more realistic interpolations.

As the u' band was not recorded for Mrk 841, whether or not there is excess lag in the u' band cannot be determined and this may be a target for future observations.

3.2 PyROA

A more robust CCF measurement was conducted using PyROA (Donnan et al. 2023). The analysis package takes a Bayesian MCMC approach to fit the light curves, where the light curves are first modeled using a running optimal average (ROA). Each point in the resulting light curve model is an inverse-variance weighted average of the data within a time window function, which reduces the weight of the data points far outside the time window of interest. PyROA fits the model to determine the mean and RMS of each light curve, the width of the ROA time window (Δ), and the lag between each of the light curves. Two-way interpolation was used, where the reference band was first interpolated and the correlation measured and then the subsidiary bands were interpolated and measured, with the final CCF being calculated from the two measurements. This is done because the alternative would result in a not strictly symmetric autocorrelation function, which is what is required from its definition as an even function.

PyROA was used to fit the entire 2016 March-2017 August dataset jointly, with all light curves fitted simultaneously, shown in Fig. 5.

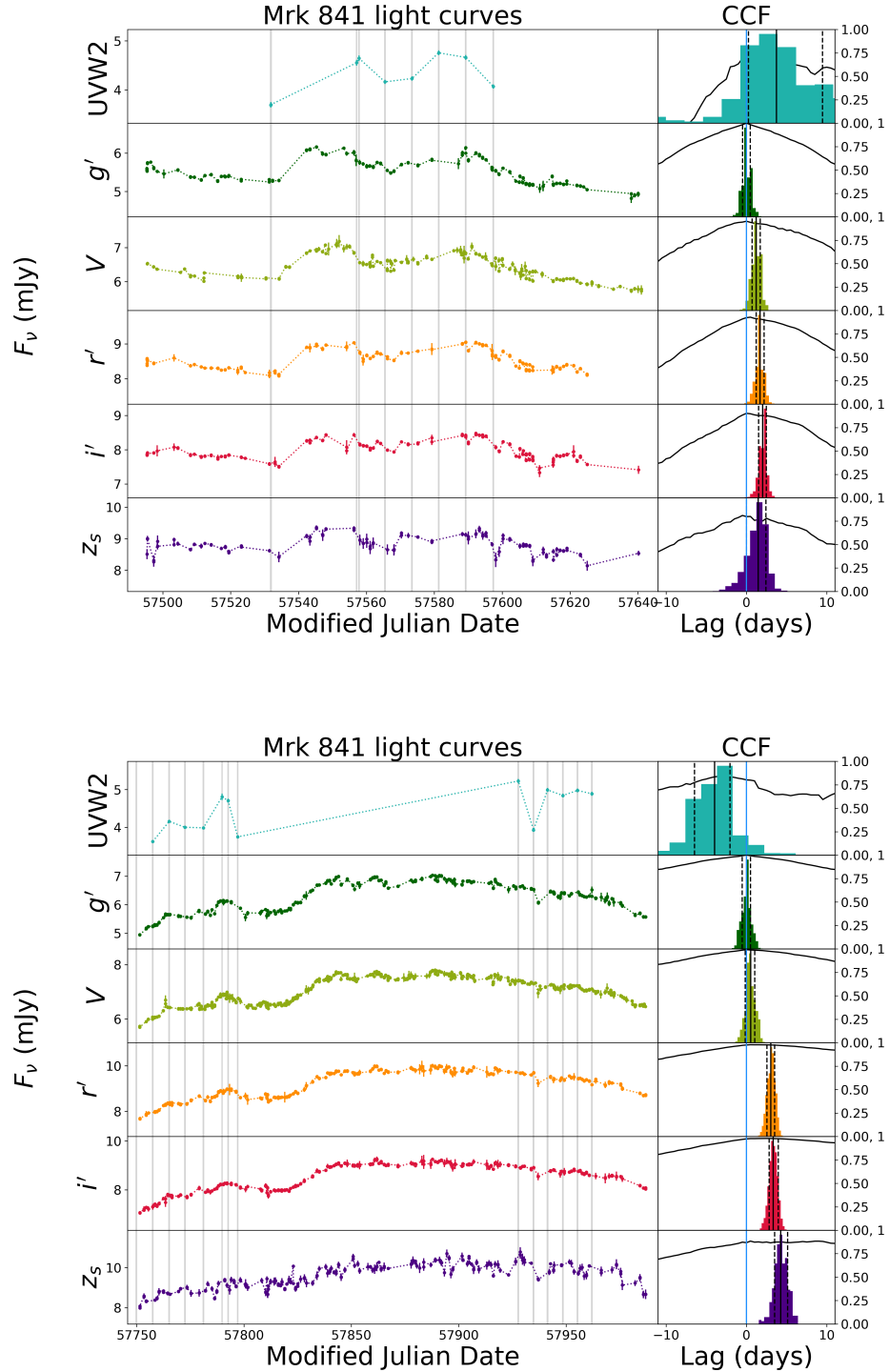


Figure 4. Top plot: Light curves, CCF, and centroid distribution for each observed band of Mrk 841 during 2016 March and 2016 September. Bottom plot: Light curves, CCF, and centroid distribution for each observed band of Mrk 841 during 2016 December and 2017 September. Left: *Swift* UVOT and LCO light curves ordered by wavelength, with UVW2 from UVOT and the rest from the LCO. Grey bands denote *Swift* XRT observation times. Right: CCFs (in black; scale on the right) and FR/RSS centroid distributions (in colour) for each band relative to the g' band, which has a reference lag of 0 shown in blue. A positive value means that the compared band lags behind g' . The median of the distribution and its 1σ confidence intervals are shown as black solid and dashed vertical lines, respectively.

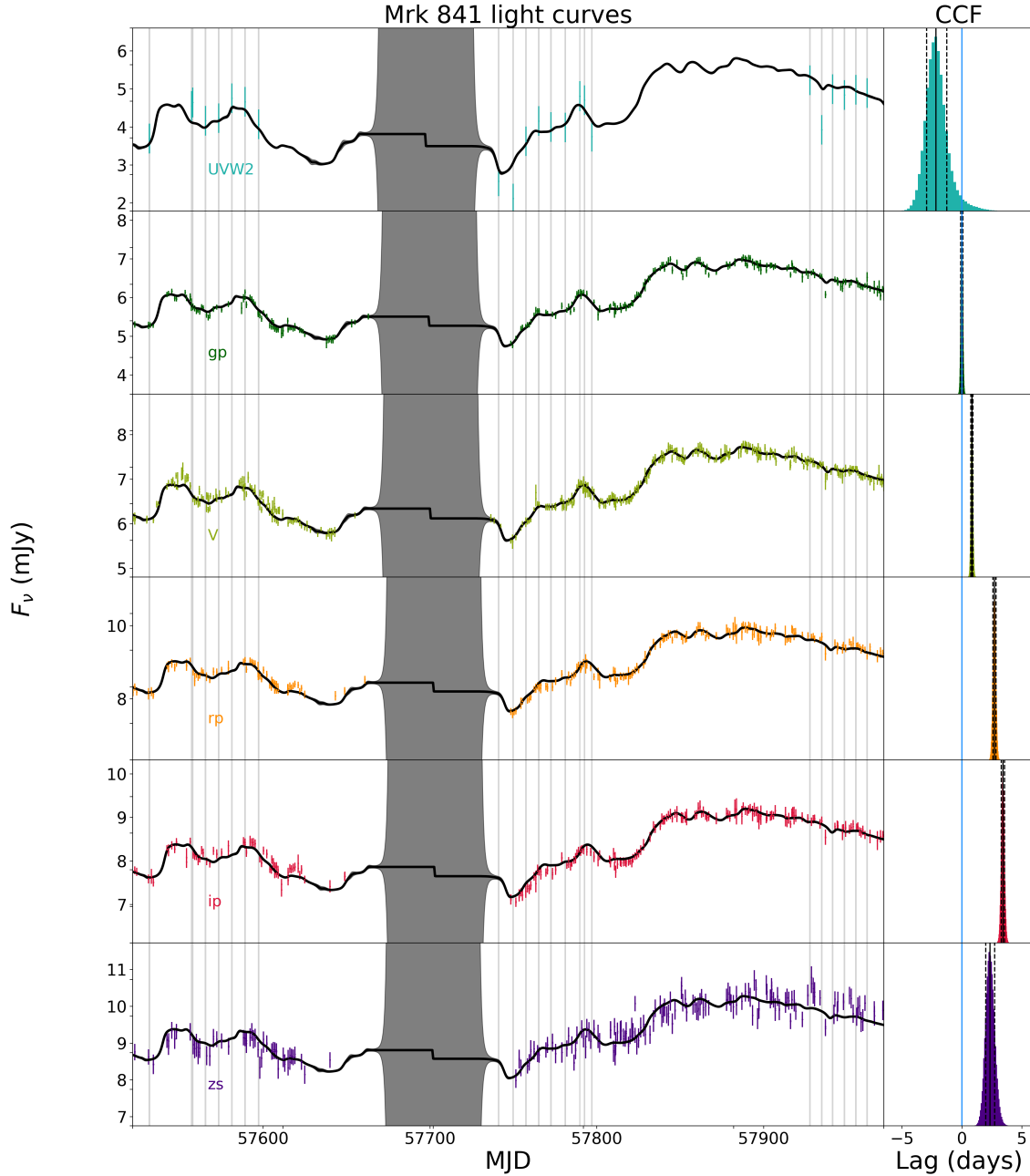


Figure 5. Left: *Swift* UVOT and LCO light curves ordered by wavelength, with UVW2 from UVOT and the rest from the LCO. Grey vertical lines denote *Swift* XRT observation times. The dark grey shading denotes the uncertainty of the fitted ROA curve (black). During the period of no observation between 2016 September and 2016 December, the uncertainty is artificially inflated to be infinite. Right: PyROA CCFs (in black; scale on the right) and FR/RSS centroid distributions (in colour) for each band relative to the g' band, which has a reference lag of 0 shown in blue. A positive value means that the compared band lags behind g' . The median of the distribution and its 1σ confidence intervals are shown as black solid and dashed vertical lines, respectively.

3.2.1 Frequency resolved lags

It was found that the choice of Δ used significantly affected the resulting lag spectrum, most noticeably in the UVW2 band and z_s band. This has been shown in previous studies, with long-term variations significantly impacting the measured lag (e.g. McHardy et al. 2014, 2018; Pahari et al. 2020; Vincentelli et al. 2021). This is most likely due to the assumption that light curves are simply shifted, smoothed, and scaled versions of the original light curve emitted from the corona. This is most visible in the z_s band of this dataset especially, where contamination from the host galaxy is most prevalent and the light curve is the most smoothed.

I find that the calculated Δ , when left as a free parameter, tends to optimise to be far too small. As a result, the “optimised” Δ tends to fit noise in the z_s band to true variations in the g' band. This results in a too-small lag measured for the z_s band and thus an apparent downturn in the lag spectrum. This phenomenon was only encountered once before for NGC 4151, by Gonzalez-Buitrago et al. (2024) and subsequently disproven by Myles (2024). Fixing Δ to larger values helps reduce this issue up to a point, as shown in the frequency-dependent time lag spectrum Fig. 6. This figure shows that with increasing Δ , the z_s band tends to plateau with the i' band. Additionally, there is a general increase of lag times across all bands, with the exception of g' as it is by necessity fixed to zero as the reference. This is likely because the accretion disc transfer function, how the input signal is distributed across radius, is asymmetric and shows a tail at long lags (e.g. Cackett et al. 2007; Starkey et al. 2015; Cackett et al. 2022).

With an increasing choice of Δ , the light curve is more and more smoothed, suppressing the fast component’s variability. Thus, with increasing Δ , I tune PyROA to be more sensitive to the slow variations in the light curve, which originate from the tail of the disc transfer function. These are likely coming from more distant reprocessors such as the BLR. Thus, the slow variations are likely to have originated from larger radii and naturally, longer lags (e.g. Cackett et al. 2022).

In fact, at longer time scales, the BLR completely dominates the variability, as seen in Fig. 5 of Cackett et al. (2022). With increasing time window Δ (and therefore, lower frequency), this must mean that more and more of the BLR is considered, as it is generally accepted that the accretion disc is closer to the corona of the AGN than the BLR. With an increasing radius R being sampled with an increasing Δ , this then naturally means that the BLR DCE begins to make an increasing impact. This is most evident in the apparent plateau in the lag spectrum at the i' and z_s bands in Fig. 6, where the BLR diffuse continuum drops

significantly at the Paschen edge (8200 Å). What also occurs is that the UVW2 band also appears to ‘flip’ in lag, switching from occurring before the g' band lag to happening after. This is perhaps the influence of the BLR DCE having a greater and greater impact at increased Δ and thus completely overwhelming the accretion disc power law.

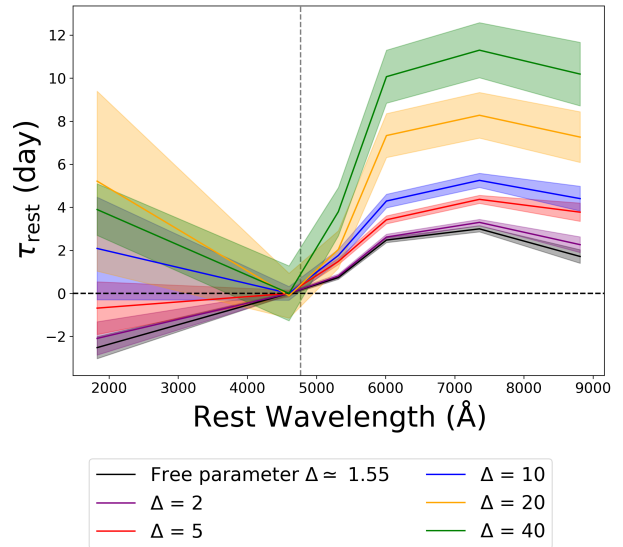


Figure 6. Frequency-resolved lag spectrum using different values of Δ in PyROA (Donnan et al. 2023). The dotted horizontal line denotes $\tau = 0$ for zero lag whilst the vertical dotted line marks λ_0 , which in this case is the g' band at 4770 Å. As Δ increases, the calculated lag spectrum also increases, owing to the asymmetrical nature of the transfer function (Starkey et al. 2015). What is also clear is that the z_s band, now smoothed from the increased Δ , tends to plateau with the i' band, thus implying a strong influence from the BLR.

4 DOES MRK 841 HAVE A “TOO-LARGE” DISC?

Having obtained the lag spectrum in Section 3, I now attempt to fit two models: the pure-disc model where the lag spectrum is parameterised as a power law as well as a combination model that considers both the diffuse continuum emission (DCE) from the BLR as well as the power law-modelled disc. This is done because through these model fittings, I can retrieve τ_0 , the time taken for light to travel from the corona of the AGN to the radius where λ_0 is emitted (in this case, the g' band). This is then easily convertible into a measure of the disc radius through $R = \tau_0 c$. In this way, the size of the accretion disc of Mrk 841 can be measured, allowing for a greater understanding of its geometry.

4.1 Disc model

The pure-disc model as seen in Eq. 4 is fitted to the lag spectrum of Mrk 841 using LMFIT (Newville et al. 2015), as seen in Fig. 7. There are three different kinds of fit, one where X was left as a free parameter, one where $X = 2.49$ for a more realistic flux-weighted radius R and λ relation (assuming $T \propto R^{-3/4}$ as in Shakura & Sunyaev (1973)), and one where $X = 4.97$ for a more simplistic R and λ relation dependent on Wien's Law.

As shown in Fig. 7, neither choice of X fits the least-squares-minimised X optimised by LMFIT, and even then, the "best"-fit fails to explain the z_s band lag.

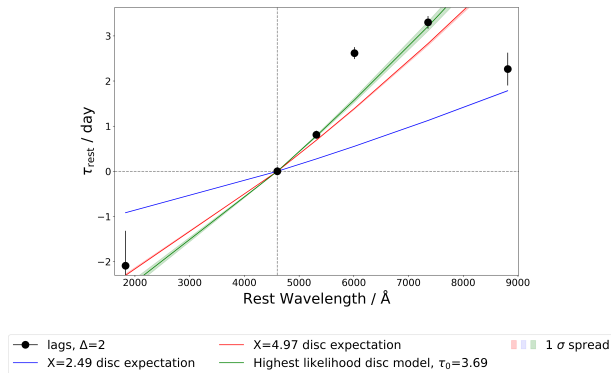


Figure 7. Delay spectrum of Mrk 841 fitted with three variations on the pure disc model Eq. 4. The three variations are due to either the choice of X : left as a free parameter and folded under τ_0 (green), $X = 2.49$ (blue), or $X = 4.97$ (orange). Each model has its 1σ spread (shaded in green, blue and orange respectively). The horizontal dotted line denotes τ_0 for zero lag and the vertical dotted line marks $\lambda_0 = 4770\text{\AA}$ for the g' band.

Following Fausnaugh et al. (2016), τ_0 can then be calculated through Eq. 4, assuming $\eta = 0.1$ and $\kappa = 1$. The Eddington luminosity is calculated using $L_{\text{Edd}} = 4\pi GM_{\text{BH}}cm_p/\sigma_T$, and the chosen X . $\dot{M}_E = L_{\text{bol}}/L_{\text{Edd}}$ is the Eddington fraction, as seen in Cackett et al. (2021).

Using this τ_0 , a straightforward calculation of the absolute size of the disc at λ_0 can be made, as τ_0 is simply the light travel time from the corona to the radius in the disc that λ_0 originated from. Table 1 shows the different calculations of τ_0 depending on the choice of X as well as the observed τ_0 computed when fitting the model $\tau_0 [(\lambda/\lambda_0)^{4/3} - 1]$ to the observed lag spectrum.

Comparing the more realistic $X = 2.49$, which considers a flux-weighted radial response, the observed $\tau_{0,\text{obs}}$ is about ~ 3 times larger, meaning that the observed accretion disc radius is also about ~ 3 times larger than what would be predicted. The less realistic choice of $X = 4.97$ yields a predicted τ_0 that is more similar to what is observed, but still too small.

	$X = 2.49$	$X = 4.97$	Observed
τ_0 (day)	1.291 ± 0.005	3.23 ± 0.02	3.7 ± 0.1
$\tau_{0,\text{obs}}/\tau_0$	2.86 ± 0.09	1.14 ± 0.04	1.0

Table 1. The calculated τ_0 (day) depending on the choice of X as well as the observed τ_0 obtained when fitting the model $\tau_0 [(\lambda/\lambda_0)^{4/3} - 1]$ to the observed lag spectrum. Also shown is the ratio of the observed $\tau_{0,\text{obs}}$ to each τ_0 .

Thus, the pure disc model is not sufficient to explain the lag spectrum of Mrk 841. Therefore, the geometry of Mrk 841 is not that of a simple standard thin accretion disc that can be parameterised as a power law. So, when trying to describe Mrk 841 in the radius where UV/optical lags originate, it is not sufficient to say that it can be modeled as an accretion disc—there is something missing that cannot be explained through a simple power law or adjustments thereof.

4.2 Diffuse continuum emission from the BLR

The missing “something” must therefore be non-disc contributions to the optical reverberation signal of Mrk 841. This must be included to fully account for the variability observed, especially in the z band. I interpret the discrepancies from the simple power law seen in Fig. 7 as the contribution from the DCE from the BLR due to free-free and free-bound hydrogen transitions (e.g. Korista & Goad 2001). The effect of the BLR on the lag spectrum is especially apparent on the Paschen (8204 Å) edge in the optical range (Korista & Goad 2019). While the effect of the BLR is also traditionally felt on the Balmer (3646 Å) edge as well, I do not have data in the u' band to analyse and cannot report on any u' band excess that is generally apparent in other AGNs (e.g. Korista & Goad 2019; Myles 2024).

Fig. 8 presents a physically motivated fit to the observed lag spectrum based on the work by Korista & Goad (2019), who modelled NGC 5548. The DCE lag spectrum contribution from the BLR (top panel in their Fig. 6) is scaled following the radius-luminosity relation $R_{\text{BLR}} \propto L^{1/2}$, where the ratio of the luminosity difference between NGC 5548 and Mrk 841 was $L_{\text{AGN}}/L_{\text{NGC5548}} \simeq 4.4$. This is done to reflect the difference between the size of the BLR of the two AGNs. Following Korista & Goad (2019), the disc lag spectrum and the luminosity-scaled DCE lag spectrum is then mixed according to the following Eq. 5:

$$\tau(\lambda) - \tau(\lambda_0) = \tau_{\text{disc}} \left(\frac{\lambda}{\lambda_0} \right)^\beta \frac{1-x}{1-Ax} + \tau_{\text{DCE}}(\lambda) \frac{(1-A)x}{1-Ax} - \tau_0, \quad (5)$$

where τ_{disc} is the disc continuum lag at $\lambda = \lambda_0$, β is the power-law index of the disc lag spectrum, $\tau_{\text{DCE}}(\lambda)$

is the DCE lag spectrum of NGC 5548 scaled by $L^{1/2}$ to the luminosity of Mrk 841, x is the fractional contribution of the DCE to the total light in the band, A is a constant to be determined, and τ_0 is the total (disc+DCE) lag at $\lambda_0 = 4770\text{\AA}$.

This parameterisation is chosen because the DCE contribution of Mrk 841 cannot be directly estimated from spectral contribution. Thus, the measured delays are fitted as a function of wavelength using the scaled template and optimising over x and A , which are left as free parameters. Five-parameter model fits for A, x, β, y_0 , and $\log \dot{m}_{\text{Edd}}$ were performed using the Python LMFIT package (Newville et al. 2015). I also use an MCMC procedure with EMCEE (Foreman-Mackey et al. 2013) to sample the posterior parameter distribution, the marginalised posterior distributions for each parameter is shown in Table 2. M_{BH} was fixed using $\log M_{\text{BH}}/M_{\odot} = 8$ from Castelló-Mor et al. (2017), after I found that leaving M_{BH} as a free parameter did not significantly alter the fit. The resulting overall fit and contributions from the accretion disc power law and BLR DCE with their respective $1-\sigma$ error envelopes are shown for each choice of X in Fig. 8 and their parameters given in Table 2. The fit resultant from not assuming any X is shown in Fig. 9 with the parameters given in Tab. 4. The joint and posterior distributions are shown in Figures A1 and A2.

Using this disc+BLR model of the lag spectrum, the influence of the power law disc lag spectrum is significantly reduced, suggesting that the BLR does have a great effect on Mark 841. Going back to the problem of the “too-large” disc size of Mrk 841 compared to the predicted sizes, Table 4 shows the predicted τ_0 using the combined disc+BLR model compared against the observed τ_0 .

	$X = 2.49$	$X = 4.97$	Observed
τ_0 (day)	1.0 ± 0.1	2.6 ± 0.4	2.035 ± 0.004
$\tau_{0,\text{obs}}/\tau_0$	2.035 ± 0.2	0.78 ± 0.1	1.0

Table 3. The calculated τ_0 (day) from the combined disc+BLR model as well as the observed τ_0 obtained when fitting the power law model $\tau_0 [(\lambda/\lambda_0)^{4/3} - 1]$ with the BLR to the observed lag spectrum. Also shown is the ratio of the observed $\tau_{0,\text{obs}}$ to each τ_0 .

What theoretically occurs is that the BLR DCE inclusion results in a less biased measurement of the disc size, thus resulting in a smaller observed τ_0 that is not so strained to fit the lag spectrum. As Table 4 shows, the ratios are much closer to unity. This indicates that the BLR DCE is indeed an important contributor to the lag spectrum and thus an important component of the geometry of Mrk 841. As it contributes so heavily to the lag spectrum, it is likely that the BLR of Mrk 841 is quite close to the accretion disc, congruent with the standard AGN model seen in

Fig 1. Further analysis of the BLR in Mrk 841 can be found in the work done by Brotherton et al. (2020).

For this disc+BLR model, the overall lag spectrum is almost entirely determined by the DCE, with the power law disc lag spectrum playing a very small role, as seen in Figures 8 and 9. This perhaps indicates that the BLR DCE component may solve a very large portion of the problem when it comes to other AGN that have measured “too-large” disc continuum lags. Table 4 shows qualitatively that including the BLR DCE provides a better representation of the measured lag spectrum, at least for Mrk 841.

Interestingly, the choice of X appears to not matter very much at all, with the parameters in Table 2 being essentially the same. This report cannot distinguish between the two regimes and so I cannot say for certain whether the flux-weighted radial response or the radius-wavelength relation according to Wien’s law is the more correct of the two.

Whilst the parameterisation in Eq. 5 simply uses a scaling of AGN NGC 5548 as a proxy for the DCE contribution, assuming that Mark 841 has the same wavelength dependence, this analysis shows that the inclusion of the DCE provides a better representation of the measured lag spectrum. However, this assumption may not necessarily be the case and a detailed modelling of the DCE in Mark 841 and their affect on the lag spectrum and SED may be needed. However, that is beyond the scope of this report and will be deferred to future analysis.

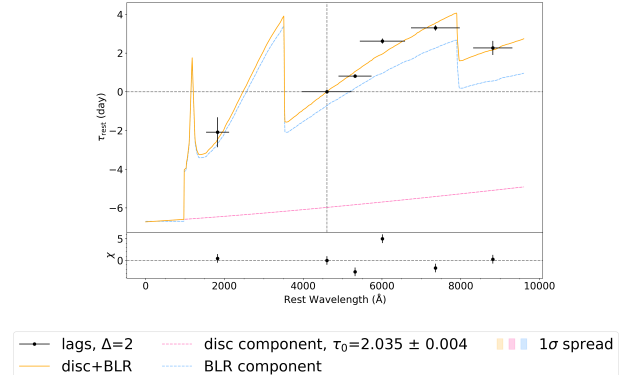


Figure 9. Top: Lag spectrum fit using $\tau_0 [(\lambda/\lambda_0)^{4/3} - 1]$ for the power law representing the accretion disc combined with the scaled DCE BLR model for NGC 5548 (orange). The individual model components, the scaled NGC 5548 DCE BLR model (blue dashed line) and the accretion disc power law model (pink dashed line) are also shown. 1σ uncertainties are shown with shaded regions in the respective colours. Bottom: Normalised residuals χ calculated by (data-model)/uncertainty. The dotted grey horizontal line denotes $\chi = 0$. As can be seen, the combined BLR+disc model is capable of explaining the apparent “downturn” of the z_s band. With this, it can be speculated that the effect of the DCE BLR in Mrk 841 is quite strong and the accretion disc, modeled by a power law, plays a much smaller role in explaining the lag spectrum.

	A	x	β	y_0	$\log \dot{m}_{\text{Edd}}$
$X = 2.49$	0.4 ± 0.3	0.7 ± 0.2	$1.35^{+0.05}_{-0.06}$	$0.5^{+0.4}_{-0.3}$	-1.1 ± 0.2
$X = 4.97$	0.4 ± 0.3	0.7 ± 0.2	1.34 ± 0.06	0.5 ± 0.3	-1.1 ± 0.2

Table 2. Marginalised posterior distribution for the parameters A , x , β , y_0 , and $\log \dot{m}_{\text{Edd}}$ for each choice of X when fitting the combined disc+BLR models seen in Fig. 8. As seen in Eq. 5, $\log \dot{m}_{\text{Edd}}$ parameterises τ_{disc} and τ_0 . When the \pm sign is used, it indicates that although the positive and negative errors were calculated separately, they round to the same figure.

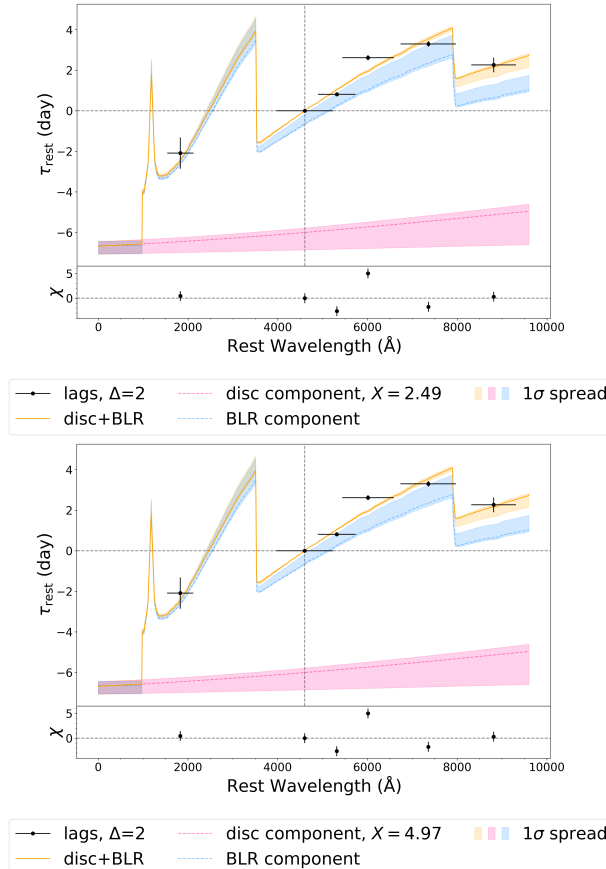


Figure 8. Top plot: Lag spectrum fit using $X = 2.49$ for the power law representing the accretion disc. Bottom plot: Lag spectrum fit using $X = 4.97$ for the power law representing the accretion disc. Top subplots: Lag spectrum using $\Delta = 2$, fitting a combined model of the scaled DCE BLR model for NGC 5548 and a power law representing the accretion disc (orange). The individual model components, the scaled NGC 5548 DCE BLR model (blue dashed line) and the accretion disc power law model (pink dashed line) are also shown. 1σ uncertainties are shown with shaded regions in the respective colours. Bottom subplots: Normalised residuals χ calculated by (data-model)/uncertainty. The dotted grey horizontal line denotes $\chi = 0$. The model fit appears to be insensitive to the choice of X .

5 SPECTRAL ANALYSIS

Light curves can be used to determine the spectral energy distribution (SED) of the variable constant flux using the flux-flux analysis method (e.g. McHardy et al. 2018; Hernández Santisteban et al. 2020; Cackett et al. 2023). This was achieved using PyROA’s FluxFlux method (Donnan et al. 2023).

Similarly to the method presented in Cackett et al. (2023), the observed light curves were first dereddened assuming Galactic absorption of $E(B - V) = 0.032$ mag (Kumar et al. 2023) and a Cardelli et al. (1989) extinction law $R_V = 3.1$. The flux densities are also corrected to the rest frame through the relation $f_\lambda/(1+z)^3$ where $z = 0.0364$ (Brotherton et al. 2020). The light curves were fitted with a linear model using a dimensionless light curve $X(t)$ that is normalised to have a mean of 0 and standard deviation of 1. This was then used to calculate a model light curve for each band,

$$f_\lambda(\lambda, t) = A_\nu(\lambda) + S_\nu(\lambda)X(t), \quad (6)$$

where $A_\nu(\lambda)$ is a constant and $S_\nu(\lambda)$ is a scale factor. This uses the assumption that the variability in each band is a shifted and scaled version of the dimensionless driving light curve $X(t)$ and there is no change in the shape of the SED of the variable component.

$S_\nu(\lambda)$ gives the RMS spectrum of the variable component of the light curves. $A_\nu(\lambda)$ is calculated from the best-fitting flux-flux relation at $X(t) = X_g$ and the maximum and minimum SEDs are determined at $X(t) = X_B$ and X_F respectively. The flux-flux relations are shown in Fig. 10 and resulting SED in Fig. 11. The average spectrum follows very well the relation $f_\lambda \propto \lambda^{-1/3}$ expected for an accretion disk. As expected, the host galaxy contamination is quite significant at optical wavelengths, especially in the z_s band.

It has been noted that the variable component in the AGN is contaminated by other additional elements such as the BLR and emission-line contribution, as seen in Fig. 8. Thus, the observed variable SED may not be the pure accretion disc component and deviations are expected. Since the variable SED follows $f_\lambda \propto \nu^{1/3} \propto \lambda^{-1/3}$ and does not turn over significantly at the blue end suggests that the intrinsic reddening of the continuum is not significant.

5.1 SED modeling

The spectral modeling of Mrk 841 was carried out in XSPEC v12.14.0 (Arnaud 1996). The LCOT, Swift UVOT, and Swift XRT spectra were fitted jointly, allowing for the possibility of coupling parameters. In the modeling, the redshift of Mrk 841 was set to $z = 0.0365$.

The full model used was

	A	x	β	y_0	$\log \dot{m}_{\text{Edd}}$	$\tau_0(\lambda_0 = 1)$ (day)
Observed	0.4 ± 0.3	0.7 ± 0.2	$1.35^{+0.05}_{-0.06}$	$0.5^{+0.4}_{-0.3}$	-1.1 ± 0.2	0.0000594 ± 0.0000001

Table 4. Marginalised posterior distribution for the parameters $A, x, \beta, y_0, \log \dot{m}_{\text{Edd}}$, and τ_0 (day) when using $\tau_0 [(\lambda/\lambda_0)^{4/3} - 1]$ for the power law representing the accretion disc combined with the scaled DCE BLR model for NGC 5548 seen in Fig. 9. Note that the τ_0 listed is for when the reference wavelength $\lambda_0 = 1$. When the \pm sign is used, it indicates that although the positive and negative errors were calculated separately, they round to the same figure.

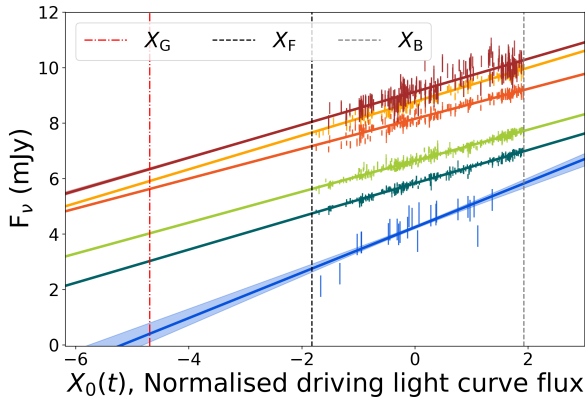


Figure 10. Flux plotted against the model driving light curve $X(t)$ for all *Swift* UVOT and LCO wave bands for Mrk 841. The vertical dotted lines show the underlying galaxy contribution (red), as well as the AGN high (X_B) and low (X_F) variable spectral flux. The best-fitting flux-flux relations are plotted as solid lines, with the 1σ uncertainty shown as shading. The value of each relation at X_G gives the value of the constant flux in each band. The slope give the strength of the variable component.

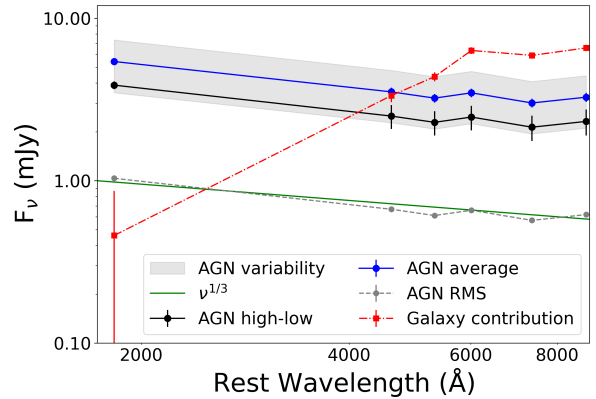


Figure 11. The UV/optical SED of Mrk 841 during 2016 March-2017 August. The variable (dotted grey) approximately follows $f_v \propto \lambda^{-1/3}$ (green) as expected from an accretion disc. The constant component (galaxy contribution) is shown in red. The SED AGN high-low (black) and the AGN average (blue) are also shown, with the 1σ AGN variability about the average plotted as grey shading.

phabs*(RELAGN+RELXILL) (Verner et al. 1996; Hagen & Done 2023; Dauser et al. 2020, respectively). phabs accounts for photoelectric absorption using cross-sections determined by Verner et al. (1996) and the hydrogen column density n_H . RELAGN is a spectral model for AGN SEDs that ranges from the optical/UV to the hard X-ray that also includes relativistic effects (Hagen & Done 2023). This model is based off of AGNSED (Kubota & Done 2018) with additional treatment of relativistic effects, including a relativistic management of accretion flow emissivity following (Novikov & Thorne 1973) (this is also done in AGNSED) and relativistic convolution ray tracing using KYCONV (Dovčiak et al. 2004). For a more detailed description, please see Hagen & Done (2023).

In the SED modeling, RELXILL was used to account for non-random variations in the residuals for the initial model of phabs*RELAGN, fitting for the Fe K α line and the Compton hump at hard X-rays. The parameters of RELXILL were also tied to those of RELAGN.

The mass of Mrk 841 is fixed at $10^8 M_{\odot}$ and the redshift z at 0.0364, thus a distance of 161.2Mpc. The spin parameter a is fixed at 0.99 for maximum

spin. The iron abundance of the disc A_{Fe} is fixed at $1.00 A_{\odot}$.

The inclination i is left at the default 60° for RELAGN, as there is no information on the inclination of Mrk 841. The electron temperature in the hot Comptonizing region is left at the default 100.00 keV for RELAGN. The emissivity of the coronal flavour models between R_{in} and R_{br} (Index1 in $r^{-\text{Index1}}$) as well as between R_{br} and R_{out} (Index2 in $r^{-\text{Index2}}$) are both left at the default value of 3.00 in the RELXILL. The observed high energy cutoff E_{cut} is fixed at the default 300.00 keV in RELXILL as none of the *Swift* X-ray spectra were captured at those energies.

Additionally, the reflection fraction in RELXILL is fixed at -1.0 to return only the reflected continuum and not the combination of both the direct continuum and the reflected continuum. This is done because RELAGN has already accounted for the direct continuum. The break radius R_{br} is fixed at -1.0 to be calculated in terms of R_{isco} , the innermost stable circular orbit of the disc as to keep the model self-consistent. R_{isco} is calculated following Page & Thorne (1974), specifically Equations 15k, 15l, and 15m. R_{br} refers to the radius at which the assumed power law of the disc breaks and changes index. This is done because of the assumed lamp post geometry of Mrk 841, consisting of a point-like source height

h above the SMBH and on the rotational axis of the SMBH. The outer radius of the accretion disc $\log R_{\text{out}}$ from RELAGN is also fixed at -1.00 to be calculated according to Laor & Netzer (1989) in terms of the self-gravity radius $R_{\text{grav}} = GM/c^2$. The outer radius parameter in RELAGN was left as a free parameter to allow the two models to be consistent with each other. The colour-temperature correction to the standard outer disc f_{col} is fixed at -1.00 to be calculated using Equations 1 and 2 in Done et al. (2012) and not as a constant correction over the entire disc.

Whilst fitting, I found that the outer radius of the warm Comptonizing region R_{warm} from RELAGN was invariant, so I report it as fixed at $6.00 R_{\text{grav}}$. R_{grav} is the gravitational radius, defined by GM_{BH}/c^2 where G is the gravitational constant, M_{BH} is the SMBH mass, and c is the speed of light. The normalisation of RELXILL was also found to be invariantly fixed at 0.00015. Additionally, the normalisation of RELAGN was fixed to be 1.00, as it accounted for the direct continuum of the disc.

The best-fit parameters of the components are provided in Table 5. These were obtained by assuming an underlying Gaussian distribution for each parameter and a diagonal covariance matrix dependent on the parameter deltas. That was done because a covariance based on the current fit was not possible. Then, using XSPEC, an MCMC procedure was performed.

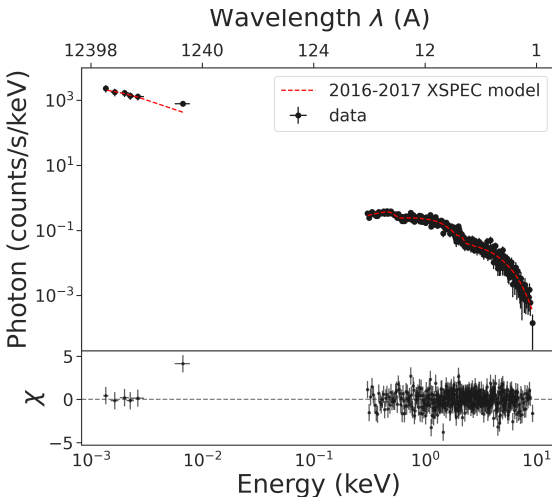


Figure 12. Top: UV/optical and X-ray spectra for the 2016 March-2017 August epoch of Mrk 841. Overplotted is the model calculated using XSPEC, phabs*(RELAGN+RELXILL). Bottom: Normalised residuals χ calculated by (data-model)/uncertainty. The dotted grey horizontal line denotes $\chi = 0$. Overall, the normalised residuals show that the given model can be used to fit very well to the data, with the exception of the UVW2 band, which appears to be far brighter than what the model can account for. This is possibly due to the lack of data gathered in the band through the *Swift* UVOT, leading to an improper calculation of the flux and therefore photon count in that band.

5.2 SED comparisons

As shown by Mehdić et al. (2023), it appears that Mrk 841 is changing its SED, much like changing-look AGNs.. Changing-look AGNs, whose SED has dramatically changed in an unphysical but still clearly possible amount of time, are thought to be due to either temporary obscuration of the object causing observational dimming and brightening or truly intrinsic variations in the emission occurring because of strong changes in the accretion rate (Ricci & Trakhtenbrot 2022). However, it is not necessarily the case that Mrk 841 is a changing-look AGN itself (Mehdić et al. 2023).

The derived SED for 2016 March-2017 August is compared to the SED models fitted by Mehdić et al. (2023) (now referred to collectively as the Mehdić models hereafter), shown in Fig. 13. The Mehdić models were extracted using WebPlotDigitizer v4.6 (Rohatgi 2022).

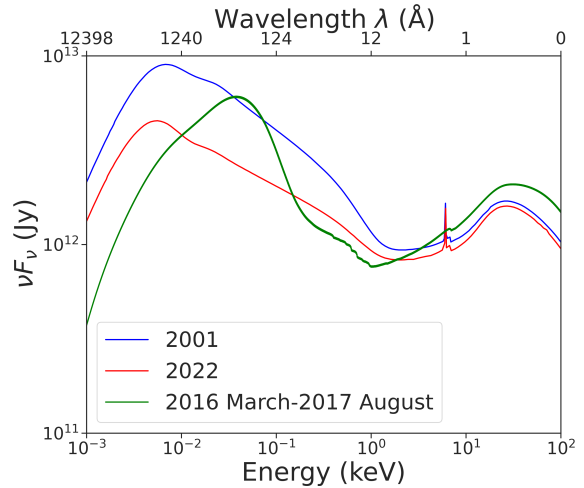


Figure 13. Derived intrinsic SED continuum model for 2016 March-2017 August (green), 2022 (blue), and 2001 (red) epochs of Mrk 841.

As seen in Fig. 13, the models chosen are not easily comparable, with large discrepancies found especially in the UV/optical part of the spectrum. For this report's derived SED, this may stem from the UVW2 band and its lack of data points to have drawn a proper flux-flux analysis from. This can be seen in Figures 4 and 5. Thus, when calculating the flux in UVW2, it is entirely possible to simply have had the PyROA decomposition fail and compute a greater flux than what was truly the case.

Another possible explanation was that perhaps the PyROA solution didn't fail and Mrk 841 does have that much flux in the UVW2 band. An explanation for that could have been that the host galaxy is star-forming, and thus Mrk 841 has an excess in the UVW2 band due to O and A stars' emissions. However, when

	Parameter
phabs	
Hydrogen column density n_{H} (10^{22} atoms cm $^{-2}$)	$0.0310^{+0.0002}_{-0.0001}$
RELAGN	
Log of SMBH mass accretion rate scaled by Eddington mass accretion rate $\log \dot{m} (\log (\dot{M}_{\text{BH}}/\dot{M}_{\text{Edd}}))$	$-1.188^{+0.008}_{-0.009}$
Electron temperature in warm Comptonizing region $T_{e,\text{warm}}$ (keV)	0.1146 ± 0.0002
Spectral index for hot Comptonizing component Γ_{hot}	1.824 ± 0.002
Spectral index for warm Comptonizing component Γ_{warm}	2.39 ± 0.01
Outer radius of hot Corona R_{hot} (R_{grav})	4.33 ± 0.02
Maximum scale-height of inner-corona H_{max} (R_{grav})	9.5735 ± 0.0009
RELXILL	
Outer radius of accretion disc R_{out} (R_{grav})	2.892 ± 0.008
Log of ionisation of accretion disc $\log x_i$	1.696 ± 0.002
C-stat/d.o.f.	561.34/660

Table 5. Best-fit parameters of components of SED model phabs*(RELAGN+RELXILL), derived from XSPEC modeling of Mrk 841. When the \pm sign is used, it indicates that although the positive and negative errors were calculated separately, they round to the same figure.

looking at the Hubble Space Telescope’s (HST) Wide Field Planetary Camera 2 (WFPC2) images of Mrk 841, an example of which is seen in Fig. 14, I find that it appears to be embedded in a very compact elliptical galaxy. Although colour was not available, it seems to be unlikely that the reason for the UVW2 excess is the amount of star-forming activity in the host galaxy as elliptical galaxies generally do not exhibit much star formation (e.g. De Lucia et al. 2006).

Thus, as seen in Figures 12 and 13, it is very possible to have miscalculated the UVW2 band to have a greater flux than what was truly the case. This calculation of the UVW2 band nevertheless shifted the peak of the fitted SED model further to higher frequencies and thus shorter wavelengths, causing the incongruent shape of the SED with the models from Mehdipour et al. (2023). It is likely that it is due to the UVW2 flux being “too-high” that the models are unable to be compared as the optical region defined by the $g'Vr'i'z_s$ bands has the same slope as the Mehdipour models but simply offset. The same reasoning can be used to rule out the *Swift* X-ray spectra, as the shape of the XSPEC model follows the same general shape as the Mehdipour models in that region.

Additionally, the χ residuals shown in Fig. 12 also indicate that the UVW2 band is an issue even if I assume that the fitted model is correct. The model cannot predict the obtained photon count of the UVW2 band even as all the other data points are reasonably well fitted.

Frustratingly, even if the UVW2 band were to be omitted, the resultant model would not be much improved. This is because the optical $g'Vr'i'z_s$ bands cover the range 4770 – 9134Å and so only charac-

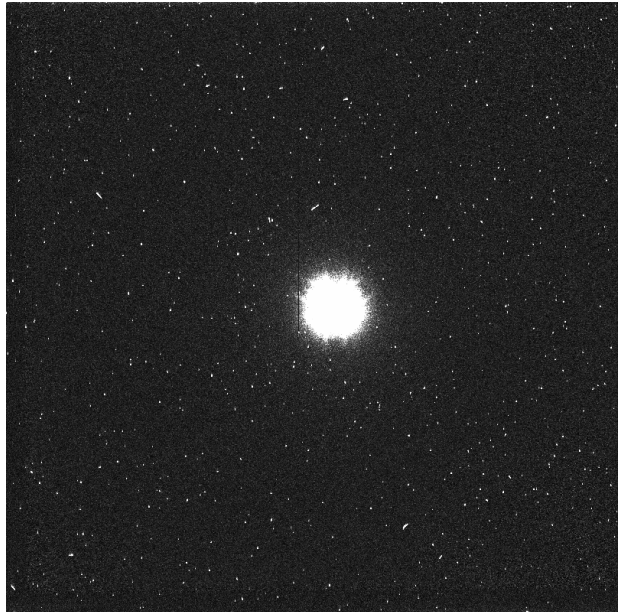


Figure 14. Image of Mrk 841 taken through the WFPC2 on HST on 1993 July 12, plotted using SAOImageDS9 (Joye & Mandel 2003). This image was accessed through the MAST Data Discovery Portal and may be obtained through <https://dx.doi.org/10.17909/za6k-s576>. As can be seen, Mrk 841 appears to be a rather compact source and clearly not a spiral disc galaxy. It is therefore unlikely to have the amount of star formation that would explain the apparent UVW2 band excess.

terise far-left slope of the model. Without additional data for higher energies and thus smaller wavelengths, the turnover of the SED cannot be characterised and the XSPEC fitting routine would be essentially running blind. It is for this reason that the problematic

UVW2 band has been allowed to remain when fitting the SED.

However, another issue arises when I consider the incoherence problem from the other direction. [Mehdipour et al. \(2023\)](#) claim that through examination of HST and OM images of Mrk 841 (see Fig. 14 for an example of a HST image), they conclude that Mrk 841 is a very compact source and so the contamination of fluxes by the host galaxy is therefore minimal, only comprising of a few percentage points. However, that is clearly not the case as seen in Fig. 11, where the host galaxy flux contamination ranges from around 10% of the observed wave band flux to entirely outshining the flux in that band, as seen in the V , r' , i' , and z_s bands. Thus, it is possible that the UV/optical range of the SED fitted by [Mehdipour et al. \(2023\)](#) is also incorrect, as they may not have properly accounted for host galaxy contamination.

This contamination would have reddened the observed fluxes in the optical bands, shifting them to be higher in wavelength, lower in energy, and thus moving the peak of the models to the left. This may also explain some part of the mismatch between the Mehdipour models and the this report's fitted model.

Another point of contention is the FeK α line that is fitted in the Mehdipour models and absent in the fitted SED model. As can be seen in Fig. 12, the residuals are generally well fitted (with one exception) and there is no apparent FeK α line to be fitted in the 2016 March-2017 August data. This may be due to the binning of the data done in XSPEC in order to plot the UV/optical data with the X-ray spectra. In XSPEC, adjacent bins are combined until they meet a significance threshold which can be provided by the user. During the fitting, I found that more stringent binning favoured the X-ray spectra, making the variations more apparent. However, that came at a severe cost to the UV/optical data which was simply combined into one bin to meet the significance threshold. In order to keep the wave bands distinct, a more lenient binning was used and in the process may have smoothed out the FeK α line in the X-ray spectra.

It is then left unclear as to what occurred during the transitional period between 2001 and 2022, due to a lack of comparable models. While some speculation can be made with the X-ray spectra, with the 2016-2017 epoch appearing to be a temporarily bright period for Mrk 841, it is not very reliable. It would be better to re-evaluate the 2001, 2016-2017, and 2022 data and fit SED models to them simultaneously as to have a clearer understanding behind the changing SED of Mrk 841, but that is left to be the subject of another paper.

6 THE GEOMETRY OF MRK 841

Through SED fitting (Section 5.1) as well lag spectrum fitting (Section 4), some conclusions on the geometry of Mrk 841 can be made.

Because I use the models RELAGN and RELXILL to fit the data, I am already assuming a specific geometry of Mrk 841. Working backwards from the assumed answer, if the models I am using provide a good fit to the data, I can then conclude that Mrk 841 has the geometry that these models describe. What then happens as I fit these models and find the best-fit parameters, I also find various measurements about Mrk 841, specifically the values shown in Table 5.

RELAGN describes a relativistic disc that has three components: a hot Comptonizing corona (which produces the X-ray tail), a warm Comptonizing puffy inner disc (which causes the soft X-ray excess), and then a standard geometrically thin optically thick accretion disc (which assumed to emit as blackbody radiation). Because of obscuration from gas absorption and dust reddening in the 10-200 eV range (e.g. [Jin et al. 2012](#)), radial stratification of the accretion flow is used. That is to say, the entirety of the accretion disc is still assumed to have relativistic Novikov-Thorne emissivity ([Novikov & Thorne 1973](#)), but this is emitted as either a blackbody, warm Comptonization, or hot Comptonization depending on the radial distance from the SMBH ([Done et al. 2012; Kubota & Done 2018](#)).

The standard disc is assumed to begin at r_{out} . In this region, up to r_{warm} , the disc is geometrically thin, optically thick, and in thermal equilibrium. At r_{warm} , the disc begins to fall out of thermal equilibrium, a key assumption of the standard disc model, and enters the warm Comptonizing region. Here, the disc becomes “puffy”, spectroscopically looking as if a warm corona were sandwiching an inner disc core ([Wielgus et al. 2022](#)). The disc then evaporates at r_{hot} into the hot Comptonizing region, where it forms a hot, optically thin, geometrically thick flow which spectroscopically forms the X-ray tail ([Hagen & Done 2023](#)). This flow then extends down to r_{isco} , at which point the geometry truncates. This is shown in Fig. 15, adapted from [Hagen & Done \(2023\)](#).

Mrk 841 could not have solely been represented by phabs*RELAGN as when that model was fitted, the residuals exhibited the characteristic variations that imply a missing reflection component, as seen in Fig. 16, even though it produced a C-stat/d.o.f. of 561.15/664. This then implies that describing Mrk 841 would not be complete without considering reflection.

RELXILL calculates the relativistic reflection spectrum from an illuminated accretion disc ([Dauser et al. 2020; García et al. 2014](#)). It assumes an empirical broken power law for the emissivity of the disc, which

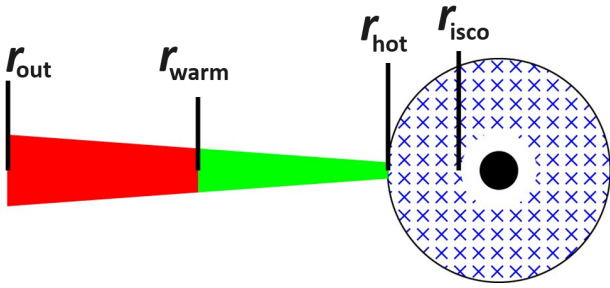


Figure 15. The RELAGN model geometry (Hagen & Done 2023) (which also uses the same geometry as AGNSED (Kubota & Done 2018), the model for which this figure was originally made). The geometry consists of a standard Shakura-Sunyaev disc (red) from r_{out} to r_{warm} . At r_{warm} , the disc enters the warm Comptonizing region (green). The disc continues down to r_{hot} , at which point the disc evaporates into the hot Comptonizing region (blue crosses). This region extends to r_{isco} , at which point it truncates.

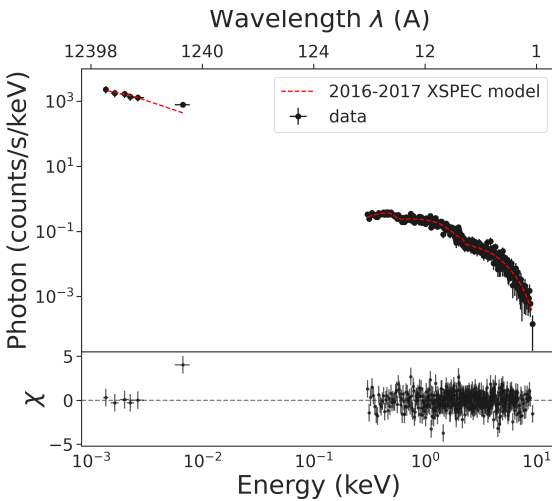


Figure 16. Top: UV/optical and X-ray spectra for the 2016 March-2017 August epoch of Mrk 841. Overplotted is the model calculated using XSPEC, phabs*RELAGN. Bottom: Normalised residuals χ calculated by (data-model)/uncertainty. The dotted grey horizontal line denotes $\chi = 0$. The residuals exhibit the characteristic variation when there is a missing reflection component.

changes at the break radius R_{br} as in RELAGN. This allows for slightly more freedom with the AGN geometry and physical location of the corona as it does not assume anything. Also as like RELAGN, it assumes that the shape of primary accretion disc continuum can be described as a simple power law with an exponential cutoff. Thus, it is well suited to be combined with RELAGN. What it adds is consideration of ionised reflection using XILLVER (García & Kallman 2010; García et al. 2013) and relativistic blurring from RELLINE (Dauser et al. 2010).

Ionising reflection refers to when X-rays are reflected off of the inner flow in the hot Comptonizing region, thus causing ionisation in the disc. A particularly convincing example of this is the Fe K α emis-

sion line, typically caused by the irradiation of less-ionised material (Fe) by a hard X-ray source which is in this case the reflection from very near the SMBH. The Fe K α line peaks at 6.4 keV and is typically a very strong line emission in AGN spectra (first noted by Mushotzky et al. 1978), although it was not able to be fitted in this report's SED modeling, the reasons of which are discussed in Section 5.2.

Relativistic blurring refers to what is observed when viewing emission from close to the SMBH, thought to be due to the relativistic motion of the material orbiting closely to the SMBH, resulting in Doppler broadening (Dauser et al. 2010). This naturally has the effect of making emission lines less distinct and more blurred.

Putting this into context, the success of adding RELXILL to the combined model means that Mrk 841 does indeed exhibit ionising reflection and relativistic blurring. It also means that Mrk 841 serves as more evidence that RELXILL is a valid train of thought to pursue, along with RELAGN.

Thus, using the geometry described by RELAGN, it can be said that Mrk 841 can be described as having a Novikov-Thorne disc that is segmented into three regimes: the hot Comptonizing region, the warm Comptonizing region, and the standard accretion disc. Additionally, it appears as though Mrk 841 has a corona that can be approximated as a point source, emitting at a maximum of $9.5735 \pm 0.009 R_{\text{grav}}$ above the SMBH.

I can also find the accretion rate of Mrk 841 to find whether Mrk 841 is accreting at sub- or super-Eddington rates, thus figuring out what models to fit next. I do this by taking the value of \dot{M}_{Edd} from Table 2, to calculate $\dot{M}_{\text{BH}} \text{ gs}^{-1}$, following the units suggested by Hagen & Done (2023). In this way, I calculate $\dot{M}_{\text{BH}} = 0.00408 \pm 0.00008$, well below the fitted $\dot{M}_{\text{Edd}} = 0.62891442 \pm 0.00000001$, meaning that Mrk 841 is accreting at sub-Eddington rates and a super-Eddington model is not required to explain Mrk 841.

Additionally, according to RELXILL, the SED of Mrk 841 should also show a strong, relativistically broadened Fe K α line as a result of hard X-rays reflecting off of the hot Comptonizing flow around R_{isco} , the self-gravitating radius of the SMBH. This also goes to show that the combined model is self-consistent: RELAGN assumes a geometry that has the hot Comptonizing flow and RELXILL produces a fit based on results that are because of said flow.

7 CONCLUSION

This report presents the results of the analysis of X-ray, UV, and optical observations of Mrk 841 during 2016 March-2017 August with the *Swift* Obser-

vatory and the ground-based LCO robotic telescope network.

The main results of the analysis of the spectral variations are as follows:

(i) The cross-correlation lag measurements for the observed UV and optical light curves cannot be adequately fitted with a pure-disc model with either choice of X governing the radius-flux response, as they both predict lags significantly smaller than what is observed.

(ii) Additionally, the lag spectrum shows evidence for the inclusion of the BLR DCE when making models. This is most evident in the Paschen jump affecting i' and z_s bands of the delay spectrum. In the case of Mrk 841, it appears that the BLR DCE is very significant, even more so than the disc even at short Δ .

(iii) The delay spectrum calculated relies a great deal upon the choice of the time window size Δ for computing the running optimal average. Increasing Δ smooths out the light curves, allowing for a less-noisy cross-correlation between bands but also smooths out the short component of the light curves' variability. This then leads to greater sensitivity to the variations of extended regions such as the BLR. Thus confirming the importance of the BLR DCE inclusion.

(iv) However, with this revelation, more work is needed to understand the slow component of the variations, namely, their origin. While there is a probability that some proportion of the slow variations are due to the BLR, it is not known for certain.

(v) SED measurements for the UV/optical fluxes decrease with wavelength in a manner compatible with the $f_\nu \propto \lambda^{-1/3}$ prediction of accretion disc theory.

(vi) However, it is quite likely that the UVW2 data used in this report was too sparse and does not yield an accurate measurement of flux when decomposed. Thus, in order to better study Mrk 841 within the period 2016 March-2017 August, it is recommended to use another source for contemporaneous UV/optical data in conjunction with LCO data.

(vii) Comparison with past and future SEDs by [Mehdipour et al. \(2023\)](#) did not yield a coherent result. To come to a true conclusion, re-evaluation of the 2001, 2016-2017, and 2022 data is needed. This will allow for a better understanding of the apparent dimming in the soft X-ray excess of Mrk 841.

(viii) I report more evidence for a three-part accretion disc model (consisting of a standard accretion disc, warm Comptonizing region, and hot Comptonizing region) that also includes ionising reflection and relativistic blurring.

ACKNOWLEDGEMENTS

This work makes use of observations from the Las Cumbres Observatory global telescope network.

This work made use of data supplied by the UK Swift Science Data Centre at the University of Leicester.

This research has made use of data and/or software provided by the High Energy Astrophysics Science Archive Research Center (HEASARC), which is a service of the Astrophysics Science Division at NASA/GSFC and the High Energy Astrophysics Division of the Smithsonian Astrophysical Observatory.

Some of the data presented in this paper were obtained from the Mikulski Archive for Space Telescopes (MAST). STScI is operated by the Association of Universities for Research in Astronomy, Inc., under NASA contract NAS5-26555. Support for MAST for non-HST data is provided by the NASA Office of Space Science via grant NNX13AC07G and by other grants and contracts.

We acknowledge with thanks the variable star observations from the AAVSO International Database contributed by observers worldwide and used in this research. This paper made use of WebPlotDigitizer (<http://arohatgi.info/WebPlotDigitizer/>) by Ankit Rohatgi.

This research made use of pandas ([McKinney 2010, 2011](#)).

This research made use of SciPy ([Virtanen et al. 2020](#)).

This research made use of ds9, a tool for data visualization supported by the Chandra X-ray Science Center (CXC) and the High Energy Astrophysics Science Archive Center (HEASARC) with support from the JWST Mission office at the Space Telescope Science Institute for 3D visualization.

This research made use of matplotlib, a Python library for publication quality graphics ([Hunter 2007](#)). This research made use of XSPEC ([Arnaud 1996](#)).

This research made use of Astropy, a community-developed core Python package for Astronomy ([Astropy Collaboration et al. 2018, 2013](#)).

This research made use of NumPy ([Harris et al. 2020](#))

REFERENCES

- Arnaud K. A., 1996, in Jacoby G. H., Barnes J., eds, Astronomical Society of the Pacific Conference Series Vol. 101, Astronomical Data Analysis Software and Systems V. p. 17
- Astropy Collaboration et al., 2013, [A&A](#), 558, A33
- Astropy Collaboration et al., 2018, [AJ](#), 156, 123
- Blandford R. D., McKee C. F., 1982, [ApJ](#), 255, 419
- Brotherton M. S., et al., 2020, [ApJ](#), 905, 77
- Brown T. M., et al., 2013, [PASP](#), 125, 1031

- Burrows D. N., et al., 2005, *Space Sci. Rev.*, **120**, 165
- Cackett E. M., Horne K., Winkler H., 2007, *MNRAS*, **380**, 669
- Cackett E. M., Bentz M. C., Kara E., 2021, *iScience*, **24**, 102557
- Cackett E. M., Zoghbi A., Ulrich O., 2022, *ApJ*, **925**, 29
- Cackett E. M., et al., 2023, *ApJ*, **958**, 195
- Cardelli J. A., Clayton G. C., Mathis J. S., 1989, *ApJ*, **345**, 245
- Castelló-Mor N., et al., 2017, *MNRAS*, **467**, 1209
- Dauser T., Wilms J., Reynolds C. S., Brenneman L. W., 2010, *MNRAS*, **409**, 1534
- Dauser T., et al., 2020, relxill: Reflection models of black hole accretion disks, Astrophysics Source Code Library, record ascl:2010.015
- Day C. S. R., Fabian A. C., George I. M., Kunieda H., 1990, *MNRAS*, **247**, 15P
- De Lucia G., Springel V., White S. D. M., Croton D., Kauffmann G., 2006, *MNRAS*, **366**, 499
- Done C., Davis S. W., Jin C., Blaes O., Ward M., 2012, *MNRAS*, **420**, 1848
- Donnan F. R., et al., 2023, *MNRAS*, **523**, 545–567
- Dovčiak M., Karas V., Yaqoob T., 2004, *ApJS*, **153**, 205
- Edelson R., et al., 2019, *ApJ*, **870**, 123
- Evans P. A., et al., 2009, *MNRAS*, **397**, 1177
- Fabian A. C., 1999, *MNRAS*, **308**, L39–L43
- Falco E., et al., 1999, *PASP*, **111**, 438–452
- Fausnaugh M. M., et al., 2016, *ApJ*, **821**, 56
- Foreman-Mackey D., Hogg D. W., Lang D., Goodman J., 2013, *PASP*, **125**, 306–312
- García J., Kallman T. R., 2010, *ApJ*, **718**, 695
- García J., Dauser T., Reynolds C. S., Kallman T. R., McClintock J. E., Wilms J., Eikmann W., 2013, *ApJ*, **768**, 146
- García J., et al., 2014, *ApJ*, **782**, 76
- Gehrels N., et al., 2004, *ApJ*, **611**, 1005
- Gonzalez-Buitrago D., et al., 2024, in prep.
- Guo W.-J., Li Y.-R., Zhang Z.-X., Ho L. C., Wang J.-M., 2022, *ApJ*, **929**, 19
- Hagen S., Done C., 2023, *MNRAS*,
- Harris C. R., et al., 2020, *Nature*, **585**, 357
- Henden A. A., Levine S., Terrell D., Welch D. L., Munari U., Kloppenborg B. K., 2018, in American Astronomical Society Meeting Abstracts #232. p. 223.06
- Hernández Santisteban J. V., 2024, in prep.
- Hernández Santisteban J. V., et al., 2020, *MNRAS*, **498**, 5399–5416
- Homayouni Y., et al., 2019, *ApJ*, **880**, 126
- Hunter J. D., 2007, Computing In Science & Engineering, **9**, 90
- Jin C., Ward M., Done C., Gelbord J., 2012, *MNRAS*, **420**, 1825
- Joye W. A., Mandel E., 2003, in Payne H. E., Jedrzejewski R. I., Hook R. N., eds, Astronomical Society of the Pacific Conference Series Vol. 295, Astronomical Data Analysis Software and Systems XII. p. 489
- King A. R., Pringle J. E., 2007, *MNRAS*, **377**, L25
- Korista K. T., Goad M. R., 2001, *ApJ*, **553**, 695
- Korista K. T., Goad M. R., 2019, *MNRAS*, **489**, 5284
- Kubota A., Done C., 2018, *MNRAS*, **480**, 1247
- Kumar S., Dewangan G. C., Singh K. P., Gandhi P., Papadakis I. E., Tripathi P., Mallick L., 2023, *ApJ*, **950**, 90
- Laor A., Netzer H., 1989, *MNRAS*, **238**, 897
- Li T., et al., 2021, *ApJ*, **912**, L29
- Longinotti A. L., Nandra K., Petrucci P. O., O'Neill P. M., 2004, *MNRAS*, **355**, 929
- Markarian B., Lipovetskii V., 1976, *Astrofizika*, p. 657
- McCully C., Turner M., Collom D., Daily M., 2022, BANZAI: Beautiful Algorithms to Normalize Zillions of Astronomical Images, Astrophysics Source Code Library, record ascl:2207.031
- McHardy I. M., et al., 2014, *MNRAS*, **444**, 1469
- McHardy I. M., et al., 2018, *MNRAS*, **480**, 2881
- McKinney W., 2010, in Proceedings of the 9th Python in Science Conference. pp 51–56
- McKinney W., 2011, Python for High Performance and Scientific Computing, 14
- Mehdipour M., Kriss G. A., Kaastra J. S., Costantini E., Mao J., 2023, *ApJ*, **952**, L5
- Mushotzky R. F., Serlemitsos P. J., Becker R. H., Boldt E. A., Holt S. S., 1978, *ApJ*, **220**, 790
- Myles K., 2024, in prep.
- Nandra K., Turner T. J., George I. M., Fabian A. C., Shrader C., Sun W. H., 1995, *MNRAS*, **273**, 85
- Netzer H., 2019, *MNRAS*, **488**, 5185
- Newville M., Stensitzki T., Allen D. B., Ingargiola A., 2015, LMFIT: Non-Linear Least-Square Minimization and Curve-Fitting for Python, doi:10.5281/zenodo.11813, <https://doi.org/10.5281/zenodo.11813>
- Novikov I. D., Thorne K. S., 1973, in Black Holes (Les Astres Occlus). pp 343–450
- Page D. N., Thorne K. S., 1974, *ApJ*, **191**, 499
- Pahari M., McHardy I. M., Vincentelli F., Cackett E., Peterson B. M., Goad M., Gültekin K., Horne K., 2020, *MNRAS*, **494**, 4057
- Peterson B. M., Horne K., 2004, *Astron. Nachr.*, **325**, 248–251
- Petrucci P. O., et al., 2006, *Astron. Nachr.*, **327**, 1043
- Petrucci P. O., et al., 2007, *A&A*, **470**, 889
- Ricci C., Trakhtenbrot B., 2022, Changing-look Active Galactic Nuclei ([arXiv:2211.05132](https://arxiv.org/abs/2211.05132))
- Rohatgi A., 2022, WebPlotDigitizer, <https://automeris.io/WebPlotDigitizer>
- Roming P. W. A., et al., 2005, *Space Sci. Rev.*, **120**, 95
- Schneider P., 2015. Springer, pp 144–148, 225, 538
- Shakura N. I., Sunyaev R. A., 1973, *A&A*, **24**, 337
- Silk J., Rees M. J., 1998, *A&A*, **331**, L1
- Starkey D. A., Horne K., Villforth C., 2015, *MNRAS*, **456**, 1960
- Sun M., Grier C. J., Peterson B. M., 2018, PyCCF: Python Cross Correlation Function for reverberation mapping studies, Astrophysics Source Code Library, record ascl:1809.005

ascl:1805.032 (ascl:1805.032)

Verner D. A., Ferland G. J., Korista K. T., Yakovlev D. G.,

1996, *ApJ*, 465, 487

Vielute R., 2024, in prep.

Vincentelli F. M., et al., 2021, *MNRAS*, 504, 4337

Virtanen P., et al., 2020, *Nat. Methods*, 17, 261

Wielgus M., et al., 2022, *MNRAS*, 514

Yu Z., et al., 2020, *ApJS*, 246, 16

APPENDIX A: CORNER PLOTS

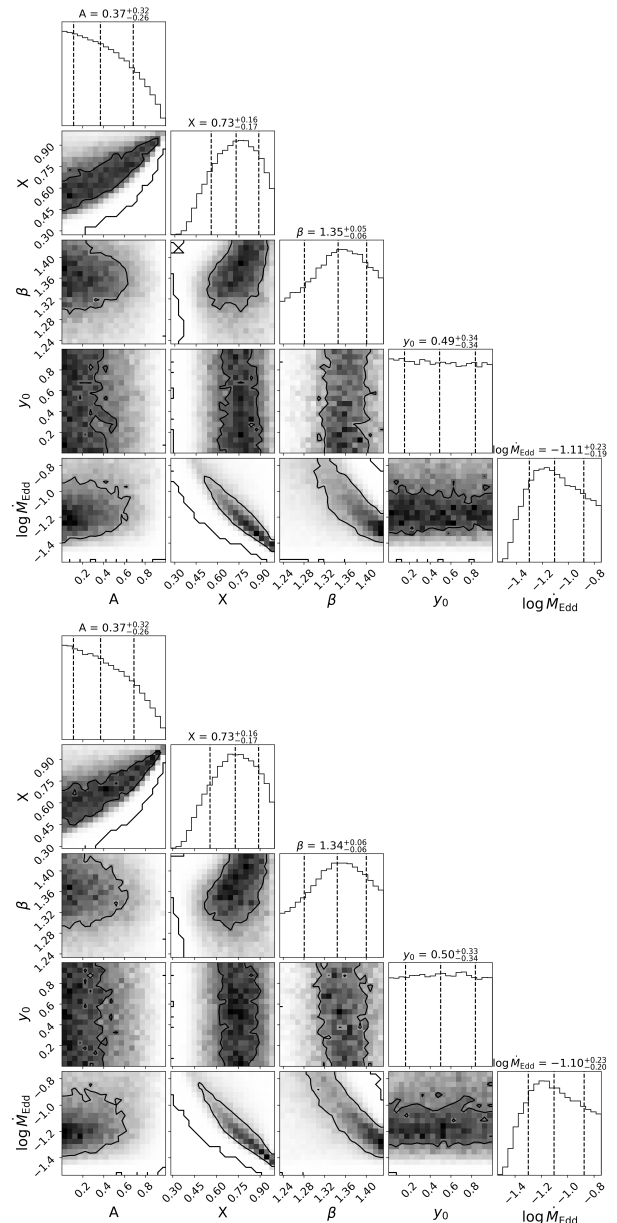


Figure A1. Top: Posterior probability distributions for lag spectrum fit of disc+BLR model with $X = 2.49$ for the accretion power law. Bottom: Posterior probability distributions for lag spectrum fit of disc+BLR model with $X = 4.97$ for the accretion power law. In all plots, contours represent the 0.5 σ and 1 σ levels. Marginal posterior distributions are shown as histograms with the median and 1 σ marked as dashed lines.

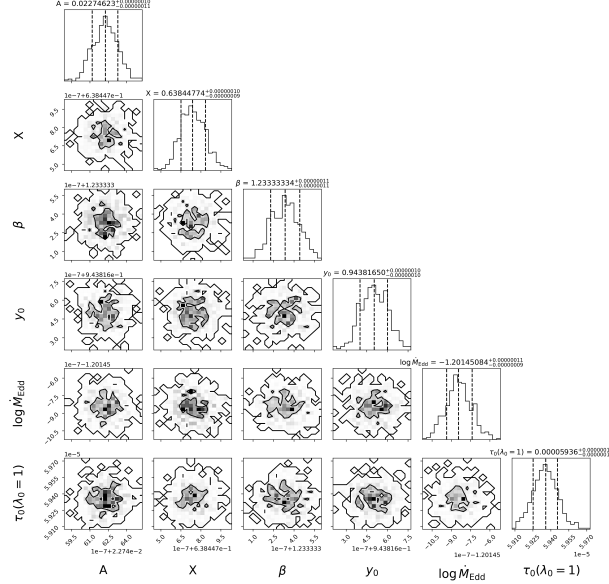


Figure A2. Posterior probability distributions for lag spectrum fit of disc+BLR model with $\tau_0 [(\lambda/\lambda_0)^{4/3} - 1]$ for the accretion power law. Contours represent the 0.5σ and 1σ levels. Note that the τ_0 shown in this plot is for when the reference wavelength $\lambda_0 = 1$. Marginal posterior distributions are shown as histograms with the median and 1σ marked as dashed lines.